Integrating Smoothing Techniques with Convolutional Neural Networks for Rice Cropping Systems Classification in Suphan Buri, Thailand

Intarat, K.[1,2,3] Tuphimai, N.[1,2*] and Jangsawang, W.[1,3]
[1]Research Unit in Geospatial Applications (Capybara Geo Lab), Faculty of Liberal Arts, Thammasat University, Thailand
E-mail: nutcha.tup@dome.tu.ac.th,* ORCID ID: https://orcid.org/0009-0004-2731-7179
[2]Department of Geography, Faculty of Liberal Arts, Thammasat University, Thailand
[3]Center of Excellence in Digital Earth Applications and Emerging Technology (CoE: DEET), Sirindhorn International Institute of Technology, Thammasat University, Thailand
Corresponding Author

DOI: https://doi.org/10.52939/ijg.v22i5.4981

Abstract
This study compares smoothing methods for classifying rice cropping systems in Suphan Buri, Thailand, using enhanced vegetation index (EVI) time series from Sentinel-2 imagery between 2023 and 2025. Three smoothing techniques: Savitzky–Golay (SG), locally estimated scatterplot smoothing (LOESS), and Gaussian smoothing are evaluated. Using continuous wavelet transform (CWT), the smoothed EVI time series are converted into a two-dimensional (2D) time-frequency representation, or scalograms. Results demonstrate that Gaussian smoothing provides the most stable and reliable representation of crop growth dynamics, achieving an overall accuracy (OA) of 0.908 and a kappa coefficient of 0.877. The classification effectively maps single crop (SC), double crop (DC), two-and-a-half crop (HC), and triple crop (TC) systems, consistent with local irrigation conditions and agricultural practices. This framework enhances the reliability of rice cropping system mapping and facilitates operational rice monitoring. It also informs crop insurance assessment and irrigation management in Thailand and other climate-constrained regions.

Keywords: Rice Cropping Systems, Enhanced Vegetation Index (EVI), Time-Series Smoothing, Continuous Wavelet Transform (CWT), Convolutional Neural Network (CNN)

1. Introduction

Rice is considered one of the most crucial crops worldwide, not only for its economic value but also for its role in global food security. It serves as a primary food source for more than 4 billion people, particularly in Asia and Southeast Asia. These regions are recognized as major rice-producing areas [1] and [2], with Asia accounting for 89.5% of global rice production in 2024 [3]. India ranks as the largest producer, followed by China, Bangladesh, Indonesia, Vietnam, Thailand, and other countries. Thailand is recognized as one of the major rice producers and exporters. The country produced more than 67 million tons of rice during the 2020/2021 crop year and ranks among the top ten rice exporters globally [3]. Additionally, many Thai farmers rely on rice cultivation as a primary source of income. The country's low-lying and fertile topography makes the central plain the most extensive rice-producing region in Thailand, accounting for more than 40% of national rice production [4]. Suphan Buri is widely regarded as one of the most important provinces for intensive rice cultivation. The land allocated to grain production, together with favorable climatic conditions in Suphan Buri, makes the area highly suitable for rice cultivation. However, effective monitoring of rice cultivation systems in intensive production areas such as Suphan Buri remains challenging due to the complex temporal dynamics of planting and harvesting cycles.

Rice cultivation systems mapping is essential for supporting crop insurance programs and efficient water resource management in regions with high seasonal variability and frequent cloud cover. Four cropping systems are commonly identified in the study area: single cropping (SC), double cropping (DC), two-and-a-half cropping (HC), and triple cropping (TC). In areas with reliable irrigation, farmers may grow rice five to six times over two

years [5], reflecting highly intensive and dynamic agricultural practices. Despite the availability of agricultural statistics and field observations, monitoring rice cropping systems remains challenging. This difficulty arises from the complex temporal variability of planting and harvesting cycles, asynchronous cultivation practices among farmers, and rapid phenological changes occurring within short time intervals. Time series of vegetation indices derived from optical satellite imagery, such as the enhanced vegetation index (EVI) and the normalized difference vegetation index (NDVI), are often affected by cloud cover and weather variability, which introduce noise and data gaps in the observations [6] and [7]. To address these limitations, smoothing methods are commonly applied to reduce noise and improve temporal continuity, allowing the vegetation signal to more accurately represent crop growth dynamics [8][9] and [10]. Different smoothing techniques have distinct theoretical foundations and characteristics. For example, the Savitzky–Golay (SG) filter preserves the overall shape of the signal while maintaining important crop growth peaks [11]. Locally estimated scatterplot smoothing (LOESS) performs well under varying noise conditions and maintains realistic crop phenology [12] and [13]. The Gaussian filter, based on a normal distribution, is effective at reducing short-term noise while preserving the general pattern of the signal [14]. However, excessive smoothing or inappropriate parameter settings may attenuate the peak of the vegetative growth stage and lead to the loss of important phenological information.

Given the limitations mentioned above, the continuity and quality of the smoothed vegetation index (VI) time series are essential for crop pattern analysis, particularly for identifying complex rice cropping cycles. In this study, three smoothing techniques (SG, LOESS, and Gaussian) are compared to evaluate their effectiveness in improving time-series quality. After applying these filters, the continuous wavelet transform (CWT) was computed from the EVI time series to generate scalograms, which represent signal information in both time and frequency domains. These scalograms were then used as inputs for a convolutional neural network (CNN) to classify rice cropping systems. The integration of CWT and CNN facilitates the extraction of detailed temporal features and improves classification performance [15][16] and [17]. Unlike many previous rice mapping studies that primarily focus on model architecture, this research systematically evaluates the influence of temporal smoothing techniques on time-series feature extraction and classification accuracy. The study specifically addresses intensive multi-cycle rice systems in tropical environments, where crop phenology is highly dynamic. By integrating temporal smoothing, CWT analysis, and CNN-based classification using Sentinel-2 EVI time series, this research provides a methodological comparison that has not been widely explored. The results offer practical insights for improving operational rice monitoring and management in Thailand, including applications in risk assessment, crop insurance compensation, and irrigation management.

2. Materials and Methods

2.1 Study Area

Suphan Buri is in the central plain of Thailand, one of the country's most important agricultural regions, as shown in Figure 1. The province lies between 14°04′–15°05′N and 99°17′–100°16′E, covering an area of 5,358.01 km² (535,801 ha), which represents approximately 5.2% of the central region. The topography is relatively flat, ranging from 3 to 10 m above mean sea level, and is characterized by fertile alluvial floodplains that are highly suitable for rice cultivation. The province receives an average annual rainfall of 1,059.9 mm, primarily occurring from May to mid-October. The province is traversed by the Tha Chin River (Suphan Buri River), which flows from north to south through the eastern part of the province and plays a crucial role in supporting rice cultivation [18]. As a result, the eastern zone of Suphan Buri benefits from well-developed irrigation systems. Rice cultivation in the province can be classified into four cropping systems: SC, DC, HC, and TC [5]. Ground-truth data were collected from rice-growing areas across the province by the Thailand Rice Science Institute (TRSI), totaling 600 sample points. The samples were evenly distributed across the four cropping systems, with 150 points per class, ensuring balanced representation and improving the model's ability to discriminate among different rice cropping patterns.

2.2 Data Collection and Preprocessing

Sentinel-2 (Level 2A) satellite imagery was used in this study due to its high spectral and spatial resolution. Surface reflectance (SR) products are generated using the Sen2Cor atmospheric correction algorithm provided by the European Space Agency (ESA). Due to the high reliability and consistency of ESA imagery, Sentinel-2 data are well suited for land-surface and vegetation monitoring applications [19] and [20]. In addition, Sentinel-2 provides pixel-level quality assurance (QA) layers, including cloud, shadow, water, and vegetation masks.

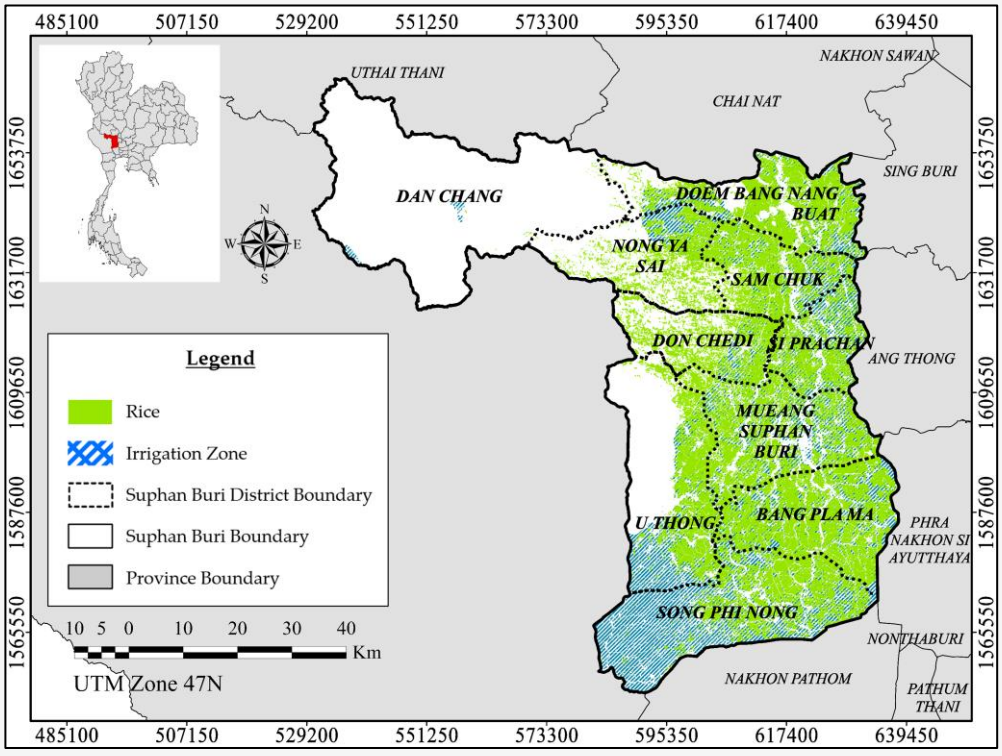

Figure 1: Suphan Buri, Thailand

These layers are essential for identifying and removing contaminated pixels before VI calculation, thereby improving the robustness and reliability of time-series analysis [20] and [21].

Sentinel-2 offers enhanced spectral capabilities, particularly in the red-edge bands, which substantially improve vegetation discrimination and the retrieval of plant biophysical parameters compared with earlier optical sensors [21] and [22]. With a high spatial resolution of 10-m and frequent revisit times, Sentinel-2 is especially suitable for monitoring agricultural variations [23] [24] and [25]. In this study, Sentinel-2 imagery was acquired between April 1, 2023, and March 31, 2025. Rice cropping systems, including both in-season and off-season cultivation, were monitored during this two-year period. The five-day revisit time of Sentinel-2 provided a total of 120 images. These satellite images were accessed and processed using the Google Earth Engine (GEE) cloud-based platform [26].

2.3 Methodology

Sentinel-2 satellite data were utilized to generate an EVI time series for classifying rice cropping systems. The extracted EVI signals were processed, employing three smoothing techniques to reduce noise while preserving seasonal phenological characteristics. The resulting signals were converted into CWT scalogram images. These scalograms served as input features for a CNN model used to classify rice cropping systems. The classification results were compared to evaluate the effectiveness of each smoothing technique. An overview of the methodological framework is presented in Figure 2.

2.3.1 Calculation of EVI

EVI was developed to improve NDVI by enhancing sensitivity to vegetative greenness and canopy density. In areas with dense vegetation, it performs well. In addition, EVI reduces the influence of atmospheric effects and background signals from soil and surface conditions. The index is calculated using the near-infrared (NIR), red, and blue spectral bands. To account for atmospheric scattering and background effects, EVI incorporates coefficients based on radiative transfer theory. As a result, EVI provides a more accurate assessment of vegetation conditions than indices based on two spectral bands, as shown in Equation 1 [27]:

$$EVI = G\frac{NIR - RED}{NIR + C_1 \cdot RED - C_2 BLUE + L}$$

Equation 1

Where:

EVI = Enhanced Vegetation Index
NIR = the surface reflectance in the near-infrared band

RED = the surface reflectance in the red band
BLUR = the surface reflectance in the blue band
G = the gain factor (typically 2.5)
C1, C2= coefficients for atmospheric resistance (commonly 6 and 7.5, respectively)
L= canopy background adjustment

The EVI time series can capture crop phenology and cropping calendars [8] [9] [28] and [29]. Vegetation indices such as EVI have been widely applied to monitor crop conditions, vegetation phenology, and seasonal dynamics, as well as to assess crop productivity [30] and [31]. Nevertheless, EVI images are often contaminated by clouds, which is a major issue in preprocessing. Cloud contamination is present in most images, especially during the rainy season. Prior to smoothing, EVI images were filtered based on pixel quality using the QA band provided with Sentinel-2 data. Cloud masking was then applied using a 50% threshold to reduce noise. Subsequently, linear interpolation was performed in both spatial and temporal domains to handle missing pixels and irregular acquisition intervals.

2.3.2 Smoothing techniques for rice time series

Time series of VIs sometimes exhibit erratic fluctuations, particularly over agricultural regions. These variations are caused by atmospheric and cloud interference [32] [33] and [34]. Such disturbances can obscure the actual seasonal patterns of rice phenology. To address the issue, smoothing methods are commonly used to reduce noise while preserving key seasonal features. Previous studies have shown that these methods can improve signal quality [32][35] and [36]. For example, EVI often exceeds 0.40 in cultivated areas during the vegetative period [37]. In this study, an EVI peak threshold of 0.4 was used to characterize single-crop rice systems. This threshold helps identify the characteristics of rice cropping and supports the identification of multiple cropping patterns. EVI time-series values were extracted for each data point from 120 images to construct rice phenological representations.

2.3.2.1 Savitzky–Golay smoothing

The SG smoothing technique applies a low-degree polynomial within a fixed-length moving window to reconstruct the VI time series using a least-squares approach. This method effectively reduces noise in the signal while preserving its shape, particularly the positions of maxima and transition points. As a result, SG is widely used in remotely sensed data to filter and reconstruct the VI time series [32][38] and [39]. The smoothed signal at time t_0 is calculated according to Equation 2:

$$\hat{y}(t_0) = \sum_{j=-m}^{m} c_j y(t_0 + j)$$

Equation 2

Where: c_f

$\hat{y}(t_0)$ = the smoothed value at time t_0
$y(t_0 + j)$ = the original observation at time $t_0 + j$
c_j = the Savitzky–Golay convolution coefficients
t_0 = the central time point
j = time offset index
m = half window size

SG smoothing method is well established in digital signal processing [36] and [40] and is known for preserving important spectral characteristics of the original signal [41]. However, the choice of window length and polynomial order is critical, as inappropriate parameter settings may lead to over-smoothing and distortion of temporal signal characteristics [41].

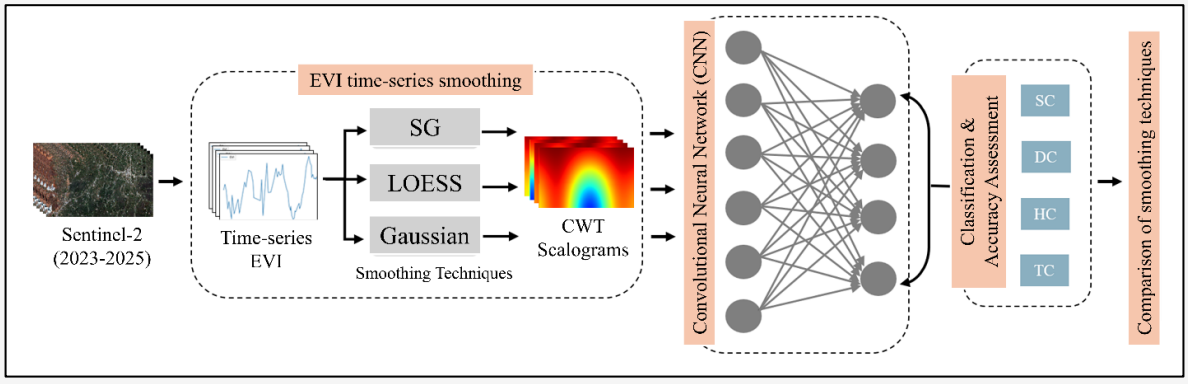

Figure 2: Workflow of rice cropping systems classification based on Sentinel-2 EVI time-series data

2.3.2.2 Locally estimated scatterplot smoothing

LOESS is a non-parametric smoothing technique. It reconstructs VI time series by fitting local polynomial regressions within the neighborhood of each target point, with weights computed using a distance-based kernel [12] and [13]. Unlike global smoothing approaches, LOESS does not assume a predefined functional form for the entire series. This flexibility enables it to adapt to local variations and nonlinear patterns [12]. At each target time t_0, LOESS estimates the smoothed value by fitting a local polynomial regression using weighted least squares, as described in Equation 3:

$$\hat{\beta}(t_0) = \arg\min_{\beta} \sum_{i=1}^{n} w_i(t_0)\left(y_i + x_i^T \beta\right)^2$$

Equation 3

Where:

y_i = denotes the observed VI value
x_i = the design vector of polynomial terms at time
β = the vector of local regression coefficients
$w_i(t_0)$ = the distance-based weight centered at t_0
t_0 = the target time
n = the number of observations

LOESS is frequently applied to VI time-series smoothing and reconstruction and is particularly effective in handling noise and irregular sampling [35] and [42]. It removes noise while preserving significant phenological information. However, the performance of LOESS is sensitive to the choice of temporal span. For long-term observations, excessive smoothing may lead to the loss of phenological detail, whereas short-term spans may result in insufficient noise removal [42].

2.3.2.3 Gaussian smoothing

Gaussian smoothing involves convolving the original time series with a Gaussian kernel. Larger weights are assigned to data points near the time point of interest and decrease for more distant points, following a normal distribution. This approach reduces noise while preserving the underlying temporal trend and can be expressed as in Equation 4 and 5 [43]:

$$\hat{y}(t_0) = \sum_{i=k}^{k} y(t_0 - i)\, w(i)$$

Equation 4

Where the Gaussian weighting function is defined, as given in Equation 5:

$$w(i) = \frac{1}{\sqrt{2\pi\sigma}} \exp\left(-\frac{i^2}{2\sigma^2}\right)$$

Equation 5

Where:

$\hat{y}(t_0)$ = the smoothed value at time t_0
$y(t_0 - i)$ = the original VI value
$w_i(t_0)$ = Gaussian weight
σ = the standard deviation controlling the width of the kernel
k = the half-window size

According to Equation (5), the effectiveness of noise reduction is controlled by the smoothing parameter σ. Excessively large values may lead to the loss of important vegetation-related features, whereas small values may be insufficient to effectively suppress noise. In remote sensing, Gaussian smoothing has been applied to reduce high-frequency noise in spectral signals [6]. It has also been widely used for vegetation-related time series, including optical and SAR-based vegetation indices, to mitigate noise induced by atmospheric effects, cloud contamination, and sensor-related uncertainties [43] and [44]. Such smoothing techniques are instrumental in improving the reliability of phenological analysis [43].

2.3.2.4 Parameter selection and implementation

The EVI time series of each reference sample was processed using three smoothing techniques: SG, LOESS, and Gaussian. The parameters for each method were not determined automatically. Instead, several values within predefined ranges were tested to identify those that best represent the EVI time-series in the study area. The selection focused on each method's ability to reduce noise while preserving peak positions and crop growth periods, which are key phenological features. The parameter ranges and values selected for each smoothing method are shown in Table 1.

Table 1: Parameter settings for the smoothing methods

Method	Parameter	Meaning	Range	Study Value	Reference
SG	*w*	Window length	[7, 41]	41	[42]
	p	Polynomial order	[2, 3]	2	
LOESS	*Frac*	Local regression window	[0.1, 0.3]	0.15	[42]
Gaussian	*σ*	Smoothing strength	[2, 6]	5	[42]

These ranges were based on commonly used values reported in previous studies [42] and further adjusted to suit the study area. Final parameter values were chosen to achieve stable smoothing results while preserving the main seasonal patterns of the rice cropping systems.

2.3.3 Continuous wavelet transform

CWT is a signal-analysis technique that captures temporal variations by representing a signal in both time and frequency domains. This time–frequency analysis method is particularly well-suited for non-stationary signals where spectral properties vary over time [45] and [46]. Consequently, wavelet-based approaches have been widely applied to identify seasonal variations and complex temporal patterns in geophysical and environmental processes [47][48] and [49]. CWT is described as in Equation 6:

$$W(a,b) = \frac{1}{\sqrt{|a|}} \int_{-\infty}^{\infty} x(t)\psi^* \left(\frac{t-b}{a} \right) dt$$

Equation 6

Where:

- $x(t)$ = the EVI time-series signal at time t
- $\psi^*(\cdot)$ = the complex conjugate of the mother wavelet
- a = the scale parameter controlling frequency resolution
- b = the translation parameter representing time localization
- $W(a, b)$ = the wavelet coefficient at scale a and time b

According to Equation (6), CWT decomposes the one-dimensional EVI signal into a two-dimensional time-frequency representation. The magnitude of the wavelet coefficients reflects the distribution of signal energy across different temporal scales. Such a representation is commonly visualized as a scalogram. Since there are 600 reference points, this process generates 600 scalograms for each smoothing technique. Each scalogram is assigned a class label corresponding to the type of rice cultivation system (SC, DC, HC, or TC), providing a standardized input data format for deep learning (DL) processing. The scale range is between 1.00 and 1.30 to highlight relevant temporal variations in the EVI signal. All scalogram images are resized to 128 × 128 pixels and converted into a numeric array format. Thus, the smoothed EVI time series are transformed into scalogram representations using CWT for subsequent DL–based classification. The scalogram provides compact and informative crop growth dynamics and seasonal transitions.

2.3.4 Convolutional neural network

CNN, a DL model derived from traditional artificial neural networks (ANNs), is specifically designed for image processing and two-dimensional data representations [50]. CNNs employ convolutional and pooling layers to learn hierarchical feature representations from input data, where shared weights enable the extraction of local features through convolutional operations, and pooling layers reduce spatial dimensionality while enhancing translational invariance. Owing to these properties, CNNs can effectively recognize discriminative spatial patterns and complex structures. A key advantage of DL models over conventional machine learning approaches that rely on handcrafted features is their ability to learn feature representations directly from data [50] and [51]. CNNs have been widely applied to image-based classification tasks, including vegetation mapping and remote sensing applications, where spatial context and pattern recognition are essential for high discriminative performance [52] and [53]. Since CNNs are inherently designed to process grid-structured data, one-dimensional time-series signals must be transformed into two-dimensional representations prior to CNN-based classification [54]. In our experiment, we configured the CNN architecture for implementation as described in Tables 2 and 3. The input scalograms were split into 80:20 for training and testing, respectively. Scalograms derived from CWT capture the time–frequency characteristics of signals, enabling CNNs to effectively extract multi-scale features embedded in temporal data [15][17] and [54]. In this study, CWT was applied to transform the EVI time series into scalogram images, which were subsequently used as inputs to a CNN to classify rice cropping systems into SC, DC, HC, and TC.

2.4 Accuracy Assessment

The predicted rice cropping classes were evaluated against ground observations using established accuracy metrics to assess classification performance. The metrics employed included OA, the kappa coefficient, producer's accuracy (PA), and user's accuracy (UA). OA represents the proportion of correctly classified samples relative to the total number of validation samples and is defined in Equation 7:

$$OA = \frac{\sum_{i=1}^{k} n_{ii}}{N}$$

Equation 7

Table 2: CNN model configuration

Layer	Output Size	Filters	Kernel	Activation
Input Image	1 x 128 x 128	-	-	-
Conv2D	32 x 128 x 128	32	3x3	ReLU
MaxPooling	32 x 64 x 64	-	2x2	-
Conv2D	64 x 64 x 64	64	3x3	ReLU
MaxPooling	64 x 32 x 32	-	2x2	-
Conv2D	64 x 32 x 32	64	3x3	ReLU
Adaptive Avg Pooling	64 x 1 x 1	-	-	-
Flatten	64	-	-	-
Fully Connected	4	-	-	Softmax

Table 3: Parameters used in the CNN models

Parameter	Value
Input image size	128 x 128
Number of classes	4
Batch size	128
Optimize	Adam
Learning rate	0.001
Loss function	Cross-Entropy Loss
Number of epochs	2000
Framework	PyTorch
Hardware	GPU (CUDA supported)

To further account for agreement occurring by chance, the Kappa coefficient was calculated in Equation 8:

$$\kappa = \frac{p_0 - p_e}{1 - p_e}$$

Equation 8

PA measures the probability that a reference sample of a given class is correctly classified and is commonly used to assess omission errors, as given by Equation 9:

$$PA_i = \frac{n_{ii}}{\sum_{j=1}^{k} n_{ii}}$$

Equation 9

UA represents the probability that a sample classified into a given class actually belongs to that class on the ground and is used to evaluate commission errors, is expressed in Equation 10:

$$UA_i = \frac{n_{ii}}{\sum_{j=1}^{k} n_{ji}}$$

Equation 10

Where:

n_{ii} = the number of correctly classified samples for class i

n_{ij} = the number of reference samples of class i classified as class j

n_{ji} = the number of samples classified as class i that belong to reference class j

k = the total number of rice cropping classes

N = the total number of validation samples

p_0 = the observed agreement OA

p_e = the expected agreement by chance

2.5 McNemar's test

To compare the performance of three smoothing techniques, McNemar test was employed. This nonparametric test is commonly applied to compare the predictive performance of two models evaluated on the same dataset. It accounts for the paired nature of predictions by focusing on the disagreements between two models [55]. A contingency table is constructed to represent the samples that are correctly or incorrectly classified by each model. McNemar test can be expressed in Equation 11:

$$\chi^2 = \frac{(n_{01} - n_{10})^2}{n_{01} + n_{10}}$$

Equation 11

Where:

χ^2 = the McNemar chi-square test statistic

n_{01} = the number of samples misclassified by Model 1 but correctly classified by Model 2

n_{10} = the number of samples correctly classified by Model 1 but misclassified by Model 2

$n_{01} - n_{10}$ = the difference these discordant pairs

Equation (11) approximately follows a chi-square distribution ($\chi 2$) with one degree of freedom. When the total number of discordant pairs is small (generally fewer than 25), the exact binomial version of McNemar test is recommended [55].

3. Results and Discussion

3.1 Temporal Smoothing and Phenological Patterns

Time-series smoothing methods are extensively employed in remote sensing to mitigate the effects of atmospheric noise, cloud contamination, and time irregularities in satellite-derived EVI time series [8] and [10]. The performance of each smoothing method depends on the characteristics of the data and the intended application. Sentinel-2 satellite imagery was used in this study due to its high spatial resolution of up to 10 m, enabling detailed classification of cropping systems at the field level [23][24][25][56] and [57]. Figures 3 and 4 show the EVI time series after smoothing by SG, LOESS, and Gaussian methods, capturing the temporal and frequency patterns of rice cropping systems over two agricultural years. EVI was selected for its effectiveness in monitoring crop condition and vegetation dynamics [32] and [58].

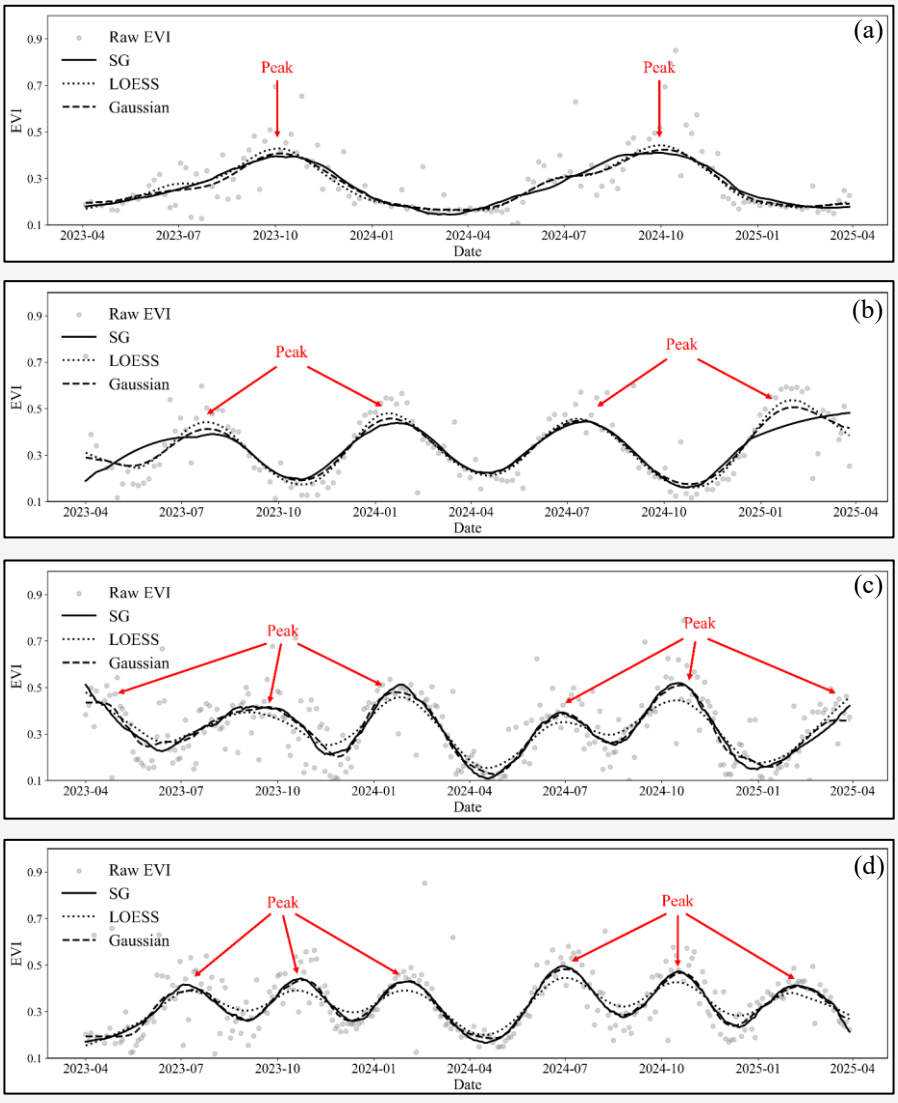

Figure 3: Raw and smoothed EVI time series using SG, Gaussian, and LOESS smoothing methods for different rice cropping systems: (a) SC, (b) DC, (c) HC, and (d) TC

Figure 3 presents smoothed EVI trajectories for SC, DC, HC, and TC systems, with gray markers representing raw data. Smoothing clarifies growth-cycle peaks for subsequent CWT feature extraction and classification. Gaussian smoothing produced broader, smoother peaks with reduced short-term variability, while SG and LOESS preserved sharper peak structures during periods of rapid growth, consistent with previous studies [6][31][32][35] and [42]. Overall, all three methods reliably captured the key phenological patterns of rice cropping systems.

3.2 Time–Frequency Characteristics from CWT

Figure 4 presents the CWT scalograms derived from the EVI time series smoothed using SG, LOESS, and Gaussian methods. The power distribution reveals distinct time-frequency patterns corresponding to the rice growth cycle. The SC system exhibits a single dominant power band, while the DC and TC systems show two and three dominant bands, respectively, reflecting increased rice-growing intensity. The HC system displays a more complex pattern with two dominant bands and weaker secondary peaks.

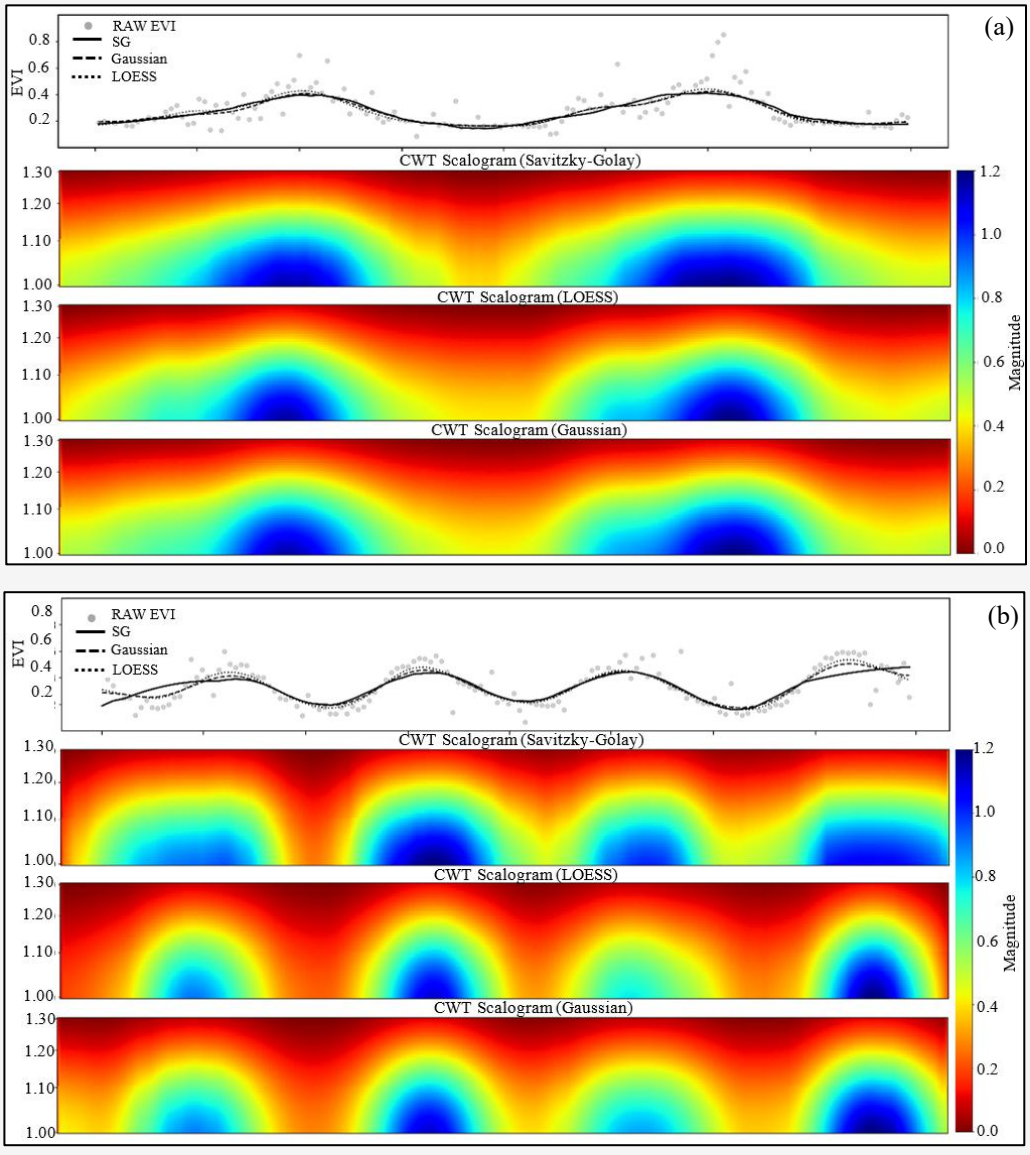

Figure 4: CWT scalograms of EVI time series smoothed using the SG, LOESS, and Gaussian methods (a) SC, and (b) DC rice cropping systems, respectively

(Continue next page)

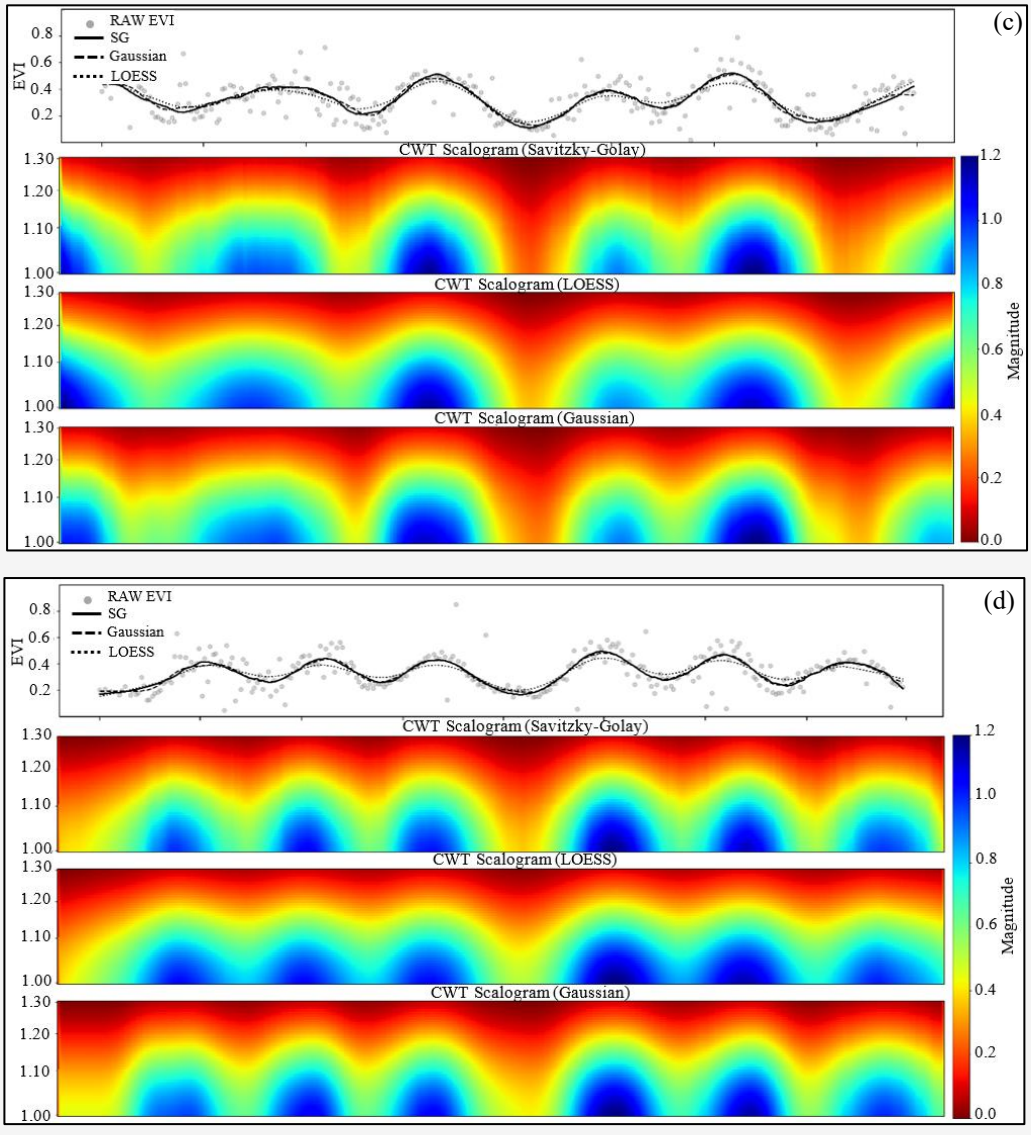

Figure 4: CWT scalograms of EVI time series smoothed using the SG, LOESS, and Gaussian methods (c) HC, and (d) TC rice cropping systems, respectively
(Continue from previous page)

Although differences in the continuity and clarity of wavelet power are noted across smoothing methods, all consistently identify the timing of the dominant power bands, corresponding to growth peaks in the smoothed EVI time series (Figure 3). This indicates that key phenological signals are preserved regardless of the smoothing technique. By transforming the one-dimensional EVI time series into a two-dimensional time-frequency representation, CWT efficiently characterizes non-stationary signals. Previous studies have demonstrated that it is particularly well suited for analyzing temporal patterns in the conventional time domain [45] and [47]. The method distinguishes growth cycles across frequency levels, which is essential for classifying rice cropping systems. Accordingly, the resulting scalograms provide a two-dimensional representation suitable for feature extraction and subsequent CNN-based classification.

3.3 Classification of Rice Cropping Systems

Although CNNs are primarily designed to learn spatial patterns from grid-structured data such as images [50] and [52], time series of vegetation indices from remote sensing data are often one-dimensional. This research transforms the EVI time series into a two-dimensional representation to accommodate the spatial learning mechanisms of CNNs [15] and [54]. The integration of the CWT–CNN framework has proven effective in agricultural

remote sensing, particularly for capturing phenological dynamics with multi-period variability [54]. Consequently, the proposed framework is a suitable and consistent strategy for mapping and classifying SC, DC, HC, and TC rice cultivation systems in Suphan Buri.

The spatial distribution of rice cropping systems shows a clear correspondence with vegetation conditions and irrigation availability (Figure 5). The classification results are consistent across the three temporal smoothing techniques (SG, LOESS, and Gaussian). SC is mainly observed in areas with limited irrigation, such as Dan Chang, Don Chedi, and Nong Ya Sai. These areas depend on rainfall and are limited to a single crop per year. In contrast, DC and TC are found in low-lying areas along the Tha Chin River, where irrigation supports multiple planting cycles. These systems are distributed across Mueang Suphan Buri, Bang Pla Ma, Song Phi Nong, U Thong, Si Prachan, Sam Chuk, and Doem Bang Nang Buat, and also occur in parts of Don Chedi and Nong Ya Sai where irrigation is available. The HC system is less extensive than the other cropping systems and is mainly concentrated in Bang Pla Ma and Doem Bang Nang Buat. Overall, the spatial distribution of rice cropping systems in the study area is influenced by rainfall patterns, irrigation infrastructure, and cultivation practices. Despite minor differences among the smoothing techniques, the overall patterns remain consistent.

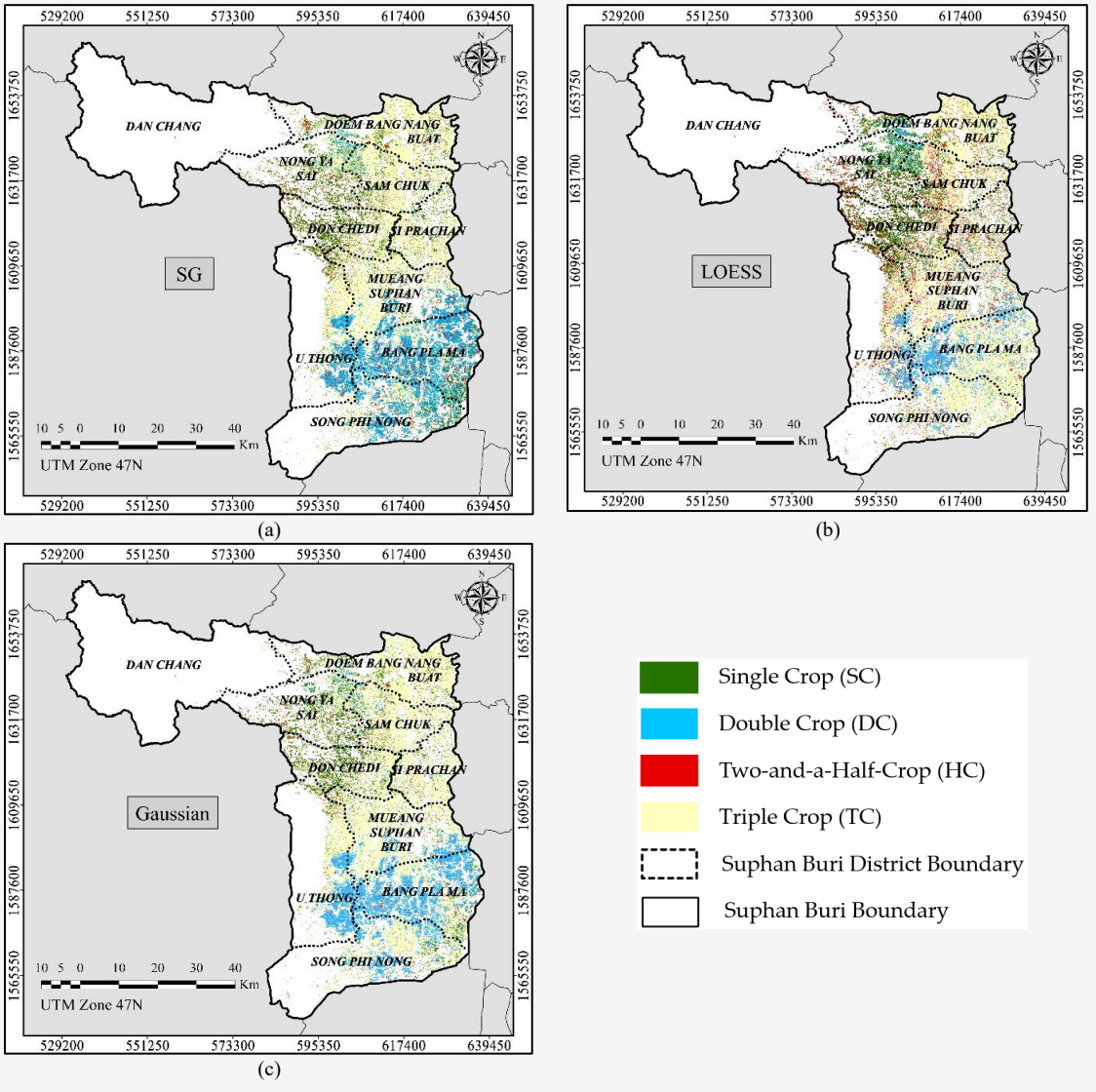

Figure 5: Spatial distribution of rice cropping systems in Suphan Buri Province during 2023–2025 using different smoothing techniques: (a) SG, (b) LOESS, and (c) Gaussian

Table 4: Accuracy assessment of the SG smoothed classification

Class	Classification result				Total
	SC	DC	HC	TC	
SC	31	1	1	0	33
DC	4	24	1	0	29
HC	0	1	24	3	28
TC	1	0	1	28	30
Total	36	26	27	31	120
Producer accuracy	0.939	0.828	0.8571	0.933	
User accuracy	0.861	0.92	0.889	0.903	
Overall accuracy	0.892				
Kappa statistics	0.855				

Table 5: Accuracy assessment of the LOESS smoothed classification

Class	Classification result				Total
	SC	DC	HC	TC	
SC	31	2	0	0	33
DC	6	22	1	0	29
HC	0	1	25	2	28
TC	0	1	0	29	30
Total	37	26	26	31	120
Producer accuracy	0.939	0.759	0.893	0.967	
User accuracy	0.838	0.846	0.962	0.936	
Overall accuracy	0.892				
Kappa statistics	0.855				

3.4 Accuracy Assessment and Data Sampling

The classification performance of the proposed CWT–CNN was evaluated using confusion matrices derived from independent validation samples. PA, UA, OA, and the Kappa coefficient were employed to assess the classification results for each smoothing technique. The results for the SG, LOESS, and Gaussian smoothed classifications are presented in Tables 3, 4, and 5, respectively. Ground-truth data were collected to support model training and validation. A total of 600 reference samples were used, evenly distributed across the four rice cropping system classes (SC, DC, HC, and TC), with 150 samples per class. In machine learning–based classification, performance is influenced more by the representativeness and balance of the training samples than by dataset size alone [59], and no universal rule exists for determining an optimal sample size [60]. Accordingly, the balanced sampling strategy adopted in this study is appropriate for parcel-level classification using Sentinel-2 imagery and ensures reliable accuracy assessment. According to Table 4, the SG smoothed classification achieved an OA of 0.892 and a Kappa coefficient of 0.855. High producer's and user's accuracies were observed for the SC and TC classes, indicating that SG smoothing effectively captured stable phenological patterns. Some confusion between HC and TC was noted, likely due to the preservation of minor growth peaks, which can lead to misinterpretation between partially overlapping and continuous cropping systems. Table 5 presents the classification accuracy assessment using the LOESS smoothing technique. The classification achieved high OA and Kappa coefficients of 0.892 and 0.855, respectively, indicating strong agreement between the predicted and reference rice cropping systems. High producer's and user's accuracies were observed for the SC and TC classes, reflecting well-defined seasonal patterns in their EVI profiles. However, the DC class exhibited the lowest producer's accuracy among all classes, suggesting increased confusion with the SC class. Minor confusion between the HC and TC classes was also observed, possibly because LOESS smoothing attenuated growth peaks.

Table 6 shows that the classification accuracy obtained using the Gaussian smoothing technique achieved the highest agreement among the evaluated methods (OA = 0.908, Kappa coefficient = 0.877), indicating strong consistency between the predicted and reference rice cropping systems. High producer's and user's accuracies were observed, reflecting stable and well-defined phenological patterns after smoothing. However, the DC class exhibited relatively lower producer's accuracy. Most misclassifications occurred between neighboring classes, particularly between SC and DC and between DC and TC, likely due to partially overlapping growth cycles among adjacent cropping systems.

Table 6: Accuracy assessment of the Gaussian smoothed classification

Class	Classification result				Total
	SC	DC	HC	TC	
SC	32	1	0	0	33
DC	4	23	1	1	29
HC	0	1	26	1	28
TC	0	1	1	28	30
Total	36	26	28	30	120
Producer accuracy	0.970	0.793	0.929	0.933	
User accuracy	0.889	0.885	0.929	0.933	
Overall accuracy	0.908				
Kappa statistics	0.877				

Table 7: Pairwise McNemar test results among smoothing techniques

Models Pair	χ^2	P-Value	95% CI	Result
SG/LOESS	2	1	[0.141, 7.099]	H_0
SG/Gaussian	1	0.625	[0.035, 3.205]	H_0
Gaussian/LOESS	2	0.688	[0.092, 2.730]	H_0

Misclassification was observed for the DC class, with some samples incorrectly assigned to other classes. This misclassification may be attributed to overlapping phenological peaks between double cropping systems and other cropping patterns in the EVI time series. The temporal profiles of DC share similar growth stages with other systems, resulting in comparable vegetation dynamics during certain periods of the season. These similarities increase the degree of overlap and reduce class separability. Additionally, variations in planting dates, harvesting times, or crop management practices may shift the timing of growth peaks, causing partial temporal overlap with other cropping systems. Consequently, some DC samples may be incorrectly assigned to neighboring classes with similar temporal signatures.

3.5 Significant Differences Between Models

To assess whether the differences in classification performance among the smoothing techniques were statistically significant, McNemar's test was conducted using pairwise comparisons between the SG, LOESS, and Gaussian methods. The results are reported in terms of the McNemar test statistic (χ^2), p-values, 95% confidence intervals, and corresponding hypothesis testing decisions. The null hypothesis (H_0) states that no statistically significant difference exists between the classification performances of the compared models at the 95% confidence level. Based on the results presented in Table 7, all pairwise comparisons yielded p-values greater than 0.05, indicating that the null hypothesis (H_0) cannot be rejected. This result suggests that the SG, LOESS, and Gaussian smoothing techniques provide comparable classification performance, with no statistically significant differences observed despite minor variations in accuracy metrics.

These findings indicate that the choice of smoothing method does not significantly influence classification performance. Although Gaussian smoothing shows slightly higher accuracy, all three approaches are similarly effective for rice cropping system classification.

4. Conclusions

This paper evaluated a CWT-CNN framework for mapping rice cropping systems in Suphan Buri, Thailand, using EVI time series derived from Sentinel-2 imagery. Three smoothing techniques (SG, LOESS, and Gaussian) were applied to the time series; their effects on signal quality and classification accuracy were systematically assessed. Results demonstrated that Gaussian smoothing provided the most stable and reliable representation of crop growth dynamics. The integration of smoothed EVI time series with the CWT-CNN framework effectively captured the temporal and frequency characteristics of vegetation dynamics, enabling accurate classification of rice cropping patterns. This framework provides a robust tool for agricultural monitoring and irrigation management. Future research could enhance the methodology by integrating Sentinel-1 SAR data.

Acknowledgments

This research was supported by the Faculty of Liberal Arts, Thammasat University, Research Unit in Geospatial Applications (Capybara Geo Lab). The authors would like to acknowledge the Rice Department and the District Agricultural Extension Office of Suphan Buri Province for providing valuable data and support for this study.

References

[1] Mohidem, N. A., Hashim, N., Shamsudin, R. and Che Man, H., (2022). Rice for food security: Revisiting its Production, Diversity, Rice Milling Process and Nutrient Content. *Agriculture*, Vol. 12(6). https://doi.org/10.3390/agriculture12060741.

[2] Bandumula, N., (2018). Rice Production in Asia: Key to Global Food Security. *Proceedings of the National Academy of Sciences, India Section B: Biological Sciences*, Vol. 88(4); 1323–1328. https://doi.org/10.1007/s40011-017-0867-7.

[3] Crops and livestock products. FAOSTAT, Food and Agriculture Organization of the United Nations. [Online]. Available: https://www.fao.org/faostat/en/#data/QCL/visualize. [Accessed: Oct. 20, 2025].

[4] Thailand Annual Statistics Book, (2024). National Statistical Office. [Online]. Available: https://www.nso.go.th/public/e-book/Statistical-Yearbook/SYB-2024/6/. [Accessed: Oct. 20, 2025].

[5] Singkawat, C. and Intarat, K., (2024). Rice Cropping Systems Classification Using Time-Series Landsat Images and Phenology-Based Algorithms in Suphan Buri, Thailand. *Asia-Pacific Journal of Science and Technology*, Vol. 29(1). https://doi.org/10.14456/apst.2024.10.

[6] Vaiphasa, C., (2006). Consideration of Smoothing Techniques for Hyperspectral Remote Sensing. *ISPRS Journal of Photogrammetry and Remote Sensing*, Vol. 60(2); 91–99. https://doi.org/10.1016/j.isprsjprs.2005.11.002.

[7] Radeloff, V. C., Roy, D. P., Wulder, M. A., Anderson, M., Cook, B., Crawford, C. J., Friedl, M., Gao, F., Gorelick, N., Hansen, M., Healey, S., Hostert, P., Hulley, G., Huntington, J. L., Johnson, D. M., Neigh, C., Lyapustin, A., Lymburner, L., Pahlevan, N., Pekel, J. F., Scambos, T. A., Schaaf, C., Strobl, P., Woodcock, C. E., Zhang, H. K. and Zhu, Z., (2024). Need and Vision for Global Medium-Resolution Landsat and Sentinel-2 Data Products. *Remote Sensing of Environment*, Vol. 300. https://doi.org/10.1016/j.rse.2023.113918.

[8] Zhang, X., Friedl, M. A., Schaaf, C., Strahler, A. H., Hodges, J. C., Gao, F., Reed, B. C. and Huete, A. R., (2003). Monitoring Vegetation Phenology Using MODIS. *Remote Sensing of Environment*, Vol. 84(3); 471–475. https://doi.org/10.1016/S0034-4257(02)00135-9.

[9] Sakamoto, T., Yokozawa, M., Toritani, H., Shibayama, M., Ishitsuka, N. and Ohno, H., (2005). A Crop Phenology Detection Method Using Time-Series MODIS Data. *Remote Sensing of Environment*, Vol. 96(3–4); 366–374. https://doi.org/10.1016/j.rse.2005.01.012.

[10] Verbesselt, J., Hyndman, R., Newnham, G. and Culvenor, D., (2010). Detecting Trend and Seasonal Changes in Satellite Image Time Series. *Remote Sensing of Environment*, Vol. 114(1); 106–115. https://doi.org/10.1016/j.rse.2009.08.014.

[11] Savitzky, A. and Golay, M. J., (1964). Smoothing and Differentiation of Data by Simplified Least Squares Procedures. *Analytical Chemistry*, Vol. 36(8); 1627–1639. https://doi.org/10.1021/ac60214a047.

[12] Cleveland, W. S., (1979). Robust Locally Weighted Regression and Smoothing Scatterplots. *Journal of the American Statistical Association*, Vol. 74(368); 829–836. https://doi.org/10.1080/01621459.1979.10481038.

[13] Cleveland, W. S., Devlin, S. J. and Grosse, E., (1988). Regression by Local Fitting: Methods, Properties, and Computational Algorithms. *Journal of Econometrics*, Vol. 37(1); 87–114. https://doi.org/10.1016/0304-4076(88)90077-2.

[14] Chung, M. K., (2020). Gaussian Kernel Smoothing. *arXiv preprint arXiv:2007.09539*. [Online]. Available: https://arxiv.org/abs/2007.09539. [Accessed: Oct. 20, 2025].

[15] Mohonta, S. C., Motin, M. A. and Kumar, D. K., (2022). Electrocardiogram Based Arrhythmia Classification using Wavelet Transform with Deep Learning Model. *Sensing and Bio-Sensing Research*, Vol. 37. https://doi.org/10.1016/j.sbsr.2022.100502.

[16] Salles, R. S. and Ribeiro, P. F., (2023). The Use of Deep Learning and 2-D Wavelet Scalograms for Power Quality Disturbances Classification. *Electric Power Systems Research*, Vol. 214. https://doi.org/10.1016/j.epsr.2022.108834.

[17] Scarpiniti, M., Parisi, R. and Lee, Y. C., (2023). A scalogram-based CNN Approach for Audio Classification in Construction Sites. *Applied Sciences*, Vol. 14(1). https://doi.org/10.3390/app14010090.

[18]Phuphaniat, M., Jeefoo, P. and Paengwangthong, W., (2024). Estimating Monthly PM2.5 Levels Using Integrated Satellite and Meteorological Data: A Case Study of Suphan Buri Province, Thailand. *Proceedings of the 2024 Geoinformatics for Spatial-Infrastructure Development in Earth and Allied Sciences (GIS-IDEAS)*, 1–4.

[19] Li, Y., Chen, J., Ma, Q., Zhang, H. K. and Liu, J. (2018). Evaluation of Sentinel-2A Surface Reflectance Derived using Sen2Cor in North America. *IEEE Journal of Selected Topics in Applied Earth Observations and Remote Sensing*, Vol. 11(6); 1997–2009. https://doi.org/10.1109/JSTARS.2018.2830403.

[20] Gascon, F., Bouzinac, C., Thépaut, O., Jung, M., Francesconi, B., Louis, J., Lonjou, V., Lafrance, B., Massera, S., Gaudel-Vacaresse, A., Languille, F., Alhammoud, B., Viallefont, F., Pflug, B., Bieniarz, J., Clerc, S., Pessiot, L., Trémas, T., Cadau, E., De Bonis, R., Claudia Isola, C., Martimort, P. and Fernandez, V., (2017). Copernicus Sentinel-2A Calibration and Products Validation Status. *Remote Sensing*, Vol. 9(6). https://doi.org/10.3390/rs9060584.

[21] Roy, D. P., Li, J., Zhang, H. K., Yan, L., Huang, H., Li, Z. and Zhang, X., (2017). Examination of Sentinel-2A Multi-Spectral Instrument (MSI) Reflectance Anisotropy and the Suitability of a General Method to Normalize MSI Reflectance to Nadir BRDF Adjusted Reflectance. *Remote Sensing of Environment*, Vol. 199; 25–38. https://doi.org/10.1016/j.rse.2017.07.030.

[22] Drusch, M., Bello, U. D., Carlier, S., Colin, O., Fernandez, V., Gascon, F., Hoersch, B., Isola, C., Laberinti, P., Martimort, P., Meygret, A., Spoto, F., Sy, O., Marchese, F. and Bargellini, P. L., (2012). Sentinel-2: ESA's Optical High-Resolution Mission for GMES Operational Services. *Remote Sensing of Environment*, Vol. 120; 25–36. https://doi.org/10.1016/j.rse.2011.11.026.

[23] Claverie, M., Ju, J., Masek, J.G., Dungan, J. L., Vermote, E. F., Roger, J., Skakun, S. and Justice, C. O., (2018). The harmonized Landsat and Sentinel-2 Surface Reflectance Data Set. *Remote Sensing of Environment*, Vol. 219; 145–161. https://doi.org/10.1016/j.rse.2018.09.002.

[24] Nwagoum, C. S. K., Yemefack, M., Tedou, F. B. S. and Oben, F. T., (2023). Sentinel-2 and Landsat-8 Potentials for High-Resolution Mapping of the Shifting Agricultural Landscape Mosaic Systems of Southern Cameroon. *International Journal of Applied Earth Observation and Geoinformation*, Vol. 124. https://doi.org/10.1016/j.jag.2023.103545.

[25] Boonma, R., Suwanprasit, C., Homhuan, S., and Shahnawaz, . (2024). Classification of Northern Thai Rice Varieties Using Random Forest (RF) and Support Vector Machine (SVM) on Google Earth Engine with Sentinel Imagery: A Case Study in Buak Khang Subdistrict, San Kamphaeng District, Chiang Mai Province. *International Journal of Geoinformatics*, Vol. 20(9), 27–42. https://doi.org/10.52939/ijg.v20i9.3539.

[26] Gorelick, N., Hancher, M., Dixon, M., Ilyushchenko, S., Thau, D. and Moore, R., (2017). Google Earth Engine: Planetary-Scale Geospatial Analysis for Everyone. *Remote Sensing of Environment*, Vol. 202; 18–27. https://doi.org/10.1016/j.rse.2017.06.031.

[27] Huete, A., Didan, K., Miura, T., Rodriguez, E. P., Gao, X. and Ferreira, L. G., (2002). Overview of the Radiometric and Biophysical Performance of the MODIS Vegetation Indices. *Remote Sensing of Environment*, Vol. 83(1–2); 195–213. https://doi.org/10.1016/S0034-4257(02)00096-2.

[28] Soontranon, N., Srestasathiern, P. and Rakwatin, P., (2015). Rice Crop Calendar Based on Phenology Analysis from Time-Series Images. *Proceedings of the 12th International Conference on ECTI-CON 2015*, 1–5. https://doi.org/10.1109/ECTICon.2015.7207029.

[29] Boonma, R., Suwanprasit, C., and Homhuan, S. (2024). Modeling Rice Growth and Yield using Integrated Remote Sensing Data on Google Earth Engine. *International Journal of Geoinformatics*,Vol. 20(11), 116–133. https://doi.org/10.52939/ijg.v20i11.3693.

[30] White, M. A., De Beurs, K. M., Didan, K., Inouye, D. W., Richardson, A. D., Jensen, O. P., O'keefe, J., Zhang, G., Nemani, R. R., Van Leeuwen, W. J. D., Brown, J. F., De Wit, A., Schaepman, M., Lin, X., Dettinger, M., Bailey, A. S., Kimball, J., Schwartz, M. D., Baldocchi, D. D., Lee, J. T . and Lauenroth, W. K., (2009). Intercomparison, Interpretation, and Assessment of Spring Phenology in North America Estimated from Remote Sensing for 1982–2006. *Global Change Biology*, Vol. 15(10); 2335–2359. https://doi.org/10.1111/j.1365-2486.2009.01910.x.

[31] Gao, Y., Wang, S., Guan, K., Wolanin, A., You, L., Ju, W. and Zhang, Y., (2020). The Ability of Sun-Induced Chlorophyll Fluorescence from OCO-2 and MODIS-EVI to Monitor Spatial Variations of Soybean and Maize Yields in the Midwestern USA. *Remote Sensing*, Vol. 12(7). https://doi.org/10.3390/rs12071111.

[32] Chen, J., Jönsson, P., Tamura, M., Gu, Z., Matsushita, B. and Eklundh, L., (2004). A Simple Method for Reconstructing a High-Quality NDVI Time-Series Data Set Based on the Savitzky–Golay Filter. *Remote Sensing of*

Environment, Vol. 91(3–4); 332–344. https://doi.org/10.1016/j.rse.2004.03.005.

[33] Zhu, Z. and Woodcock, C. E., (2012). Object-Based Cloud and Cloud Shadow Detection in Landsat Imagery. *Remote Sensing of Environment*, Vol. 118; 83–94. https://doi.org/10.1016/j.rse.2011.10.028.

[34] Ju, J. and Roy, D. P., (2008). The Availability of Cloud-Free Landsat ETM+ Data Over the Conterminous United States and Globally. *Remote Sensing of Environment*, Vol. 112(3); 1196–1211. https://doi.org/10.1016/j.rse.2007.09.022.

[35] Moreno, Á., García-Haro, F. J., Martínez, B. and Gilabert, M. A., (2014). Noise Reduction and Gap Fillingof fAPAR Time Series Using an Adapted Local Regression Filter. *Remote Sensing*, Vol. 6(9); 8238–8260. https://doi.org/10.3390/rs6098238.

[36] Luo, J., Ying, K., He, P. and Bai, J., (2005). Properties of Savitzky–Golay Digital Differentiators. *Digital Signal Processing*, Vol. 15(2); 122–136. https://doi.org/10.1016/j.dsp.2004.09.002.

[37] Galford, G. L., Mustard, J. F., Melillo, J., Gendrin, A., Cerri, C. C. and Cerri, C. E., (2008). Wavelet Analysis of MODIS Time Series to Detect Expansion and Intensification of Row-Crop Agriculture in Brazil. *Remote Sensing of Environment*, Vol. 112(2); 576–587. https://doi.org/10.1016/j.rse.2007.09.023.

[38] Cao, R., Chen, Y., Shen, M., Chen, J., Zhou, J., Wang, C. and Yang, W., (2018). A Simple Method to Improve the Quality of NDVI Time-Series Data by Integrating Spatiotemporal Information with the Savitzky–Golay Filter. *Remote Sensing of Environment*, Vol. 217; 244–257. https://doi.org/10.1016/j.rse.2018.07.022.

[39] Chen, Y., Cao, R., Chen, J., Liu, L. and Matsushita, B., (2021). A Practical Approach to Reconstruct High-Quality Landsat NDVI Time-Series Data by Gap Filling and the Savitzky–Golay Filter. *ISPRS Journal of Photogrammetry and Remote Sensing*, Vol. 180; 174–190. https://doi.org/10.1016/j.isprsjprs.2021.08.012.

[40] Schafer, R. W., (2011). What is a Savitzky–Golay Filter? *IEEE Signal Processing Magazine*, Vol. 28(4); 111-117. https://doi.org/10.1109/MSP.2011.941097.

[41] Krishnan, S. R. and Seelamantula, C. S., (2012). On the Selection of Optimum Savitzky–Golay Filters. *IEEE Transactions on Signal Processing*, Vol. 61(2); 380–391. https://doi.org / 10.1109/TSP.2012.2225050.

[42] Cai, Z., Jönsson, P., Jin, H. and Eklundh, L., (2017). Performance of Smoothing Methods for Reconstructing NDVI Time-Series and Estimating Vegetation Phenology from MODIS Data. *Remote Sensing*, Vol. 9(12). https://doi.org/10.3390/rs9121271.

[43] Hird, J. N. and McDermid, G. J., (2009). Noise Reduction of NDVI Time Series: An Empirical Comparison of Selected Techniques. *Remote Sensing of Environment*, Vol. 113(1); 248–258. https://doi.org/10.1016/j.rse.2008.09.003.

[44] Nasrallah, A., Baghdadi, N., El Hajj, M., Darwish, T., Belhouchette, H., Faour, G., Darwich, S. and Mhawej, M. (2019). Sentinel-1 Data for Winter Wheat Phenology Monitoring and Mapping. *Remote Sensing*, Vol. 11(19). https://doi.org/10.3390/rs11192228.

[45] Sadowsky, J., (1996). Investigation of Signal Characteristics Using the Continuous Wavelet Transform. *Johns Hopkins APL Technical Digest*, Vol. 17(3); 258–269.

[46] Slavič, J., Simonovski, I. and Boltežar, M., (2003). Damping Identification Using a Continuous Wavelet Transform: Application to Real Data. *Journal of Sound and Vibration*, Vol. 262(2); 291–307. https://doi.org/10.1016/S0022-460X(02)01197-1.

[47] Rhif, M., Ben Abbes, A., Farah, I. R., Martínez, B. and Sang, Y., (2019). Wavelet Transform Application for/in Non-Stationary Time-Series Analysis: A Review. *Applied Sciences*, Vol. 9(7). https://doi.org/10.3390/app9071345.

[48] Grinsted, A., Moore, J. C. and Jevrejeva, S., (2004). Application of the Cross Wavelet Transform and Wavelet Coherence to Geophysical Time Series. *Nonlinear Processes in Geophysics*, Vol. 11(5–6); 561–566. https://doi.org/10.5194/npg-11-561-2004.

[49] Tomás, R., Pastor, J. L., Béjar-Pizarro, M., Bonì, R., Ezquerro, P., Fernández-Merodo, J. A., Guardiola-Albert, C., Herrera, G., Meisina, C., Teatini, P., Zucca, F., Zoccarato, C. and Franceschini, A., (2020). Wavelet Analysis of Land Subsidence Time-Series: Madrid Tertiary Aquifer Case Study. *Proceedings of the International Association of Hydrological Sciences*, Vol. 382; 353–359. https://doi.org/10.5194/piahs-382-353-2020.

[50] Alzubaidi, L., Zhang, J., Humaidi, A. J., Al-dujaili, A., Duan, Y., Al-Shamma, O., Santamaría, J. I., Fadhel, M. A., Al-Amidie, M. and Farhan, L., (2021). Review of Deep Learning: Concepts, CNN Architectures, Challenges, Applications, Future Directions. *Journal of Big Data*, Vol. 8(1). https://doi.org/10.1186/s40537-021-00444-8.

[51] LeCun, Y. and Bengio, Y., (1998*). Convolutional Networks for Images, Speech, And Time Series.* In: The Handbook of Brain Theory and Neural Networks. MIT Press, Cambridge, MA.

[52] Kattenborn, T., Leitloff, J., Schiefer, F. and Hinz, S., (2021). Review on Convolutional Neural Networks (CNN) in Vegetation Remote Sensing. *ISPRS Journal of Photogrammetry and Remote Sensing*, Vol. 173; 24–49. https://doi.org/10.1016/j.isprsjprs.2020.12.010.

[53] Purwono, P., Ma'arif, A., Rahmaniar, W., Fathurrahman, H. I. K., Frisky, A. Z. K. and ul Haq, Q. M., (2022). Understanding of Convolutional Neural Network (CNN): A Review. *International Journal of Robotics and Control Systems*, Vol. 2(4); 739–748. https://doi.org/10.31763/ijrcs.v2i4.888.

[54] Zhao, L., Li, Q., Zhang, Y., Wang, H. and Du, X., (2019). Integrating the Continuous Wavelet Transform and a Convolutional Neural Network to Identify Vineyard Using Time Series Satellite Images. *Remote Sensing*, Vol. 11(22). https://doi.org/10.3390/rs11222641.

[55] Pembury Smith, M. Q. and Ruxton, G. D., (2020). Effective use of the McNemar Test. *Behavioral Ecology and Sociobiology*, Vol. 74(11). http://doi.org/10.1007/s00265-020-02916-y.

[56] Song, X. P., Huang, W., Hansen, M. C. and Potapov, P., (2021). An Evaluation of Landsat, Sentinel-2, Sentinel-1 and MODIS Data for Crop Type Mapping. *Science of Remote Sensing*, Vol. 3. https://doi.org/10.1016/j.srs.2021.100018.

[57] Waleed, M., Mubeen, M., Ahmad, A., Habib-Ur-Rahman, M., Amin, A., Farid, H. U., Hussain, S., Ali, M., Qaisrani, S. A., Nasim, W., Javeed, H. M. R., Masood, N., Aziz, T., Mansour, F. and El Sabagh, A., (2022). Evaluating The Efficiency of Coarser to Finer Resolution Multispectral Satellites in Mapping Paddy Rice Fields Using GEE Implementation. *Scientific Reports*, Vol. 12(1). https://doi.org/10.1038/s41598-022-17454-y.

[58] Bridhikitti, A. and Overcamp, T. J., (2012). Estimation of Southeast Asian Rice Paddy Areas with Different Ecosystems from Moderate-Resolution Satellite Imagery. *Agriculture, Ecosystems & Environment*, Vol. 146(1); 113–120. https://doi.org/10.1016/j.agee.2011.10.016.

[59] Belgiu, M. and Drăguţ, L., (2016). Random Forest in Remote Sensing: A Review of Applications and Future Directions. *ISPRS Journal of Photogrammetry and Remote Sensing*, Vol. 114; 24–31. https://doi.org/10.1016/j.isprsjprs.2016.01.011.

[60] Foody, G. M., (2002). Status of Land Cover Classification Accuracy Assessment. *Remote Sensing of Environment*, Vol. 80; 185–201. https://doi.org/10.1016/S0034-4257(01)00295-4.